Booms and Busts in the Deep

W. E. FARRELL

Science Applications International Corporation, McLean, Virginia

WALTER MUNK

Scripps Institution of Oceanography, University of California, San Diego, La Jolla, California

(Manuscript received 2 February 2010, in final form 14 April 2010)

ABSTRACT

Deep sea (5 km) pressure and velocity at the Hawaii-2 Observatory (H2O), midway between Hawaii and California, exhibit a number of remarkable features that are interpreted using the Longuet–Higgins theory of acoustic radiation from oppositely directed surface waves. A change in the slope of the bottom spectra near 5 Hz can be associated with a transition near 2.5 Hz (25-cm wavelength) of the surface wave spectrum from the classical κ^{-4} saturated (wind independent) Phillips spectrum to a distinct band of ultragravity waves. Bottom spectra are remarkably stable. Occasional 15-dB busts in the gravities and booms in the ultragravities are prominent features in the bottom records and can be associated with calms and storms at the sea surface. For strong winds, two broad lobes in the directional spectrum of the gravity waves are nearly perpendicular to the wind; as the wind drops, the lobes become narrower and more nearly aligned with the wind, leading to busts.

1. Introduction

More than a half century ago, Longuet-Higgins (1950) explained how oppositely traveling waves on the ocean surface couple to an acoustic wave of twice the frequency that interacts with the ocean bottom to cause microseisms. The theory was developed to account for far lower frequencies (such as 7-s microseisms from coastal reflection of a 14-s swell) than are of concern here, but it is still relevant (Kedar et al. 2008). The purely acoustic problem of radiation by a continuous spectrum of partially opposed waves was elegantly solved by Brekhovskikh (1966), including the effect of surface tension. More than a half dozen papers on this theory have subsequently appeared, most of which have been cast into a consistent notation by Kibblewhite and Wu (1996). However, various small numerical discrepancies in some of the published formulas were not uncovered.

Webb and Cox (1986) extended the application of the Longuet–Higgins theory up to 1-Hz surface wave frequencies and used deep sea pressure data to estimate the exponent of a $\cos^{2s}(\theta)$ directional spread function [defined in Eq. (1)]. A further order of magnitude extension by Farrell and Munk (2008) inferred an isotropic spread function for some of the spectrum. They associated a break in slope in the deep pressure spectrum at 5 Hz (long known to the acoustic community; e.g., Kibblewhite and Ewans 1985, Fig. 9) with a well-recognized wave transition at about 2.5 Hz from the classical gravity wave spectrum to the ultragravities (e.g., Heron et al. 2006, Fig. 7). Previously, we used long gravities and short gravities, but this new nomenclature avoids confusion with the length of a wave being ruled against water depth. From the viewpoint of the dispersion relation, all waves of interest here are short waves.

Here, we reinforce and extend our previous work using the year 2002 hydrophone and geophone records of the Hawaii-2 Observatory (H2O). The hydrophone, measuring pressure, has an omnidirectional sensitivity function. The geophone, measuring velocity, has a dipole sensitivity function. We have primarily studied data from the vertical geophone, which emphasizes energy arriving from overhead. The spectra are remarkably stable for the year, except for occasional gravity busts and ultragravity booms that can be associated with calms and storms above.

Our two papers, together with Webb and Cox (1986) and McCreery et al. (1993), show that deep sea pressure

Corresponding author address: W. E. Farrell, 13765 Durango Drive, Del Mar, CA 92014.
E-mail: wef@farrell-family.org

DOI: 10.1175/2010JPO4440.1

and velocity in the range $1 < f < 30$ Hz carry significant information about waves on the ocean surface above in the range $6 < \lambda < 0.017$ m. Direct oceanographic observations in the upper part of the range are difficult to make. Waves in this range are indirectly observed by scatterometers because they are the most important component of surface roughness. However, they are just one of a score of factors determining the microwave reflectivity of the sea surface and, in practice, scatterometers are calibrated under known wind conditions, not known wave conditions.

2. H2O observations

The H2O (Duennebier et al. 2002) was a suite of instruments deployed on (and slightly below) the seafloor in the eastern Pacific, at 27.9°N, 142.0°W. The ocean depth is 4947 m, and the instruments are well below the ''surface reciprocal depth'' (same sound velocity as at the surface) of 4500 m. H2O data, taken at 160 samples per second and archived at the Data Management Center of the Incorporated Research Institutions for Seismology (IRIS DMC), are available for October 1999–May 2003, inclusive.

The 2002 record (analysis of prior year's data is in progress) has been broken into 4-h windows. For a typical 0.1-Hz resolution, this gives 3000 degrees of freedom for each spectral estimate, corresponding to 95% error limits of ± 0.1 dB (Gaussian distribution). Self-noise restricts the upper frequency limit to 40 Hz for the geophone and to 10 Hz for the hydrophone (unless the wind is brisk), well below the Nyquist limit. Therefore, most of the analysis is based on the geophone data, but the consistency with the independent hydrophone data raises our confidence in the reality of the tiny deep sea oscillations and their inference about the ocean waves overhead (see discussion of Fig. 4).

The spectra for the vertical geophone have been boosted by 3 dB: the calibration file mistakenly uses the open circuit, not damped, generator constant (the error is verified through comparison with the adjacent Guralp sensor). Occasional errors in timing, gaps in data, and corrections to the time at which the gain of the hydrophone changed have been uncovered and corrected. A persistent 8-Hz tone in the hydrophone has been filtered. The seasonal occurrence of whale songs in the 15–25-Hz band has been muted. Ship passages, lasting 2–6 h, were easily detected and eliminated.

The probability density function (pdf) of log power for the whole year was calculated at a set of frequencies. At 5 Hz the distribution is close to Gaussian with a half-amplitude width of ± 0.5 dB. For frequencies less than 5 Hz, there is a long tail toward low power; for frequencies above 5 Hz, there is a long tail toward high power. In both cases, widths on the short tail (saturated) side of the distribution are similar to the 5-Hz value. The long tails are associated with the busts and booms, respectively. At ''normal'' times the spectra are notable for their steadiness.

The asymmetrical and frequency-dependent tails of the pdfs make both the mean and median, conventional measures of centrality, unsuitable for these data. Instead, we use the mode, the most likely value of the power at a given frequency.

A major part of our findings derives from the remarkable coincidence of the seafloor booms and busts with the storms and calms above. There are two sources for the surface wind data. First, there are the U_{10} data from the National Oceanographic and Atmospheric Administration (NOAA)/National Centers for Environmental Prediction (NCEP) reanalysis project (Kalnay et al. 1996). These were provided by N. Graham (2009, personal communication) for the whole year at grid point 27.62°N, 142.50°W. Second, there are the cross-calibrated multiplatform (CCMP) ocean surface wind components (Atlas et al. 2008), available from the Physical Oceanography Distributed Active Archive Center (DAAC) at the Jet Propulsion Laboratory (JPL). These were provided by B. Sperry (2009, personal communication) at the same grid point. The two datasets differ by a point-to-point scatter of about 1 m s^{-1}. This may seem slight, but the difference is not insignificant here. The probability density function of each model has a broad crest between 5 and 7 m s^{-1}, with an annual median speed of 6.5 m s^{-1}.

3. Boom and bust events

A 30-day segment of the spectrogram of both pressure and velocity is shown in Fig. 1. The vertical black lines show the boundaries between the gravity, ultragravity, and capillary waves. The three horizontal dark bands in the left portion represent troughs in the spectral intensity (named busts); the two light bands in the right portion are spectral ridges (named booms). During a boom the power is also elevated for frequencies at 1 Hz and below. Booms and busts are typically 15 dB in magnitude and both usually last several days. Booms and busts are well-defined events, and they each occupy about 10% of the yearly record. This particular month of record has been chosen because it contains several examples of both booms and busts; it is not typical of the entire year.

It is crucial to appreciate that booms and busts never intermingle. If the power is low in the gravity band, it is normal in the ultragravity band; however, when it is high in the ultragravity band, it is normal in the gravity

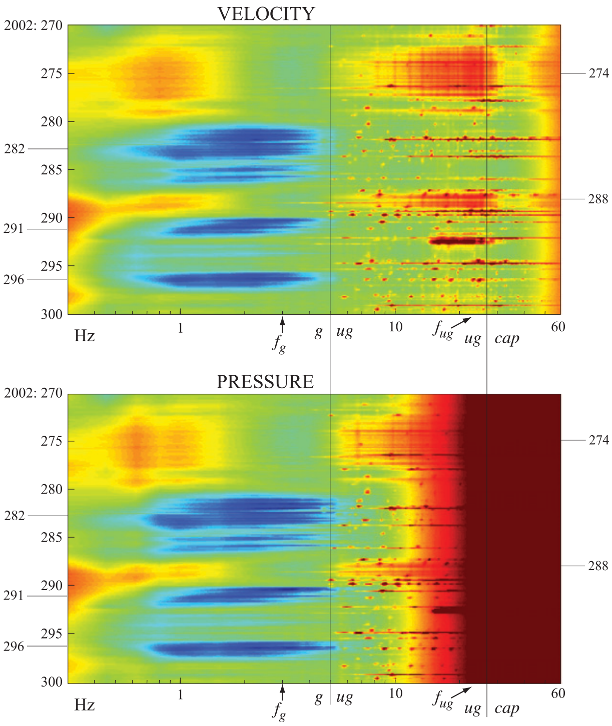

FIG. 1. Spectrograms for 2002 YD 270–300 at the seafloor, prewhitened by the annual average 3-h spectrum for $U = 6$ m s^{-1}. The range from blue to red is 40 dB. We distinguish between three distinct wave systems: traditional (Phillips) gravity waves, ultragravities, and capillaries, separated at $g|ug = 5$ Hz and $ug|\mathrm{cap} = 27.5$ Hz acoustic frequencies; 3 and 24 Hz have been selected as representative of busts and booms. Dark blue bands (labeled 282, 291, and 296 on the left) are busts. Yellowish ridges (274 and 288 on the right) are booms. (bottom) The bright red on the right side is hydrophone self-noise.

band. At times when the wind is exceptionally strong, however, the boom does cause a slight depression in the upper reaches of the gravity spectrum. Booms and busts are ubiquitous, if rare, features of the deep sea and can be recognized in prior publications (e.g., McCreery et al. (1993, Figs. 8, 10).

Normal spectrograms consist of days at a time that show a uniform plane of pale green over both bands; booms and busts are absent although seasonal whale songs and occasional ship lines cause rises in power that are readily identified. The stability of the normal spectrograms poses a major (perhaps the major) challenge in the interpretation of the deep sea signals.

Figure 2 shows the evolution of the velocity spectrum of the yearday (YD) 282 bust (left) and the YD 274 boom (right) at selected times. Labels along the lower-frequency axes identify the representative frequencies of the gravity busts and the ultragravity booms, as well as the gravity to ultragravity ($g|ug$) and ultragravity to capillary ($ug|\mathrm{cap}$) transition frequencies. Boom and bust spectra vary smoothly with time. The bust evolves over a 2-day interval of descent (top) and a 5-day recovery (bottom). The spectra for -2 and $+5$ days are virtually identical and are typical of normal spectra during the year. The boom (right column) evolved over 4 days of ascent and 4 days of recovery.

Booms and busts are highly correlated with wind speed overhead (Fig. 3, top), but the influence of wind is greatly suppressed at the 5-Hz $g|ug$ transition (Fig. 3, bottom). The top two panels clearly show the transition between saturated (U independent) and unsaturated behavior. We use the adjective saturated to mean independent of wind speed and apply it both to the ceiling of the gravity spectrum and the floor of the ultragravity. The gravity spectrum at 3 Hz is nearly constant, at about -162 dB, when the wind speed exceeds 6 m s^{-1}, and the ultragravity spectrum at 24 Hz is nearly constant, at about -198 dB, when the wind is less than 6 m s^{-1}. The wind speed causing the saturated/unsaturated transition in the bottom measurements is curiously similar for the two frequency bands. Others have noted the correlation of bottom noise with wind speed and the saturated/unsaturated behavior of bottom measurements, notably McCreery et al. (1993).

Figure 4 displays boom and bust events with reference to the normal spectra. The six curves in this figure contain the essence of an entire year's data from both hydrophone and geophone. For yearday 201, representative of a normal day, the spectra (blue) are in accord with the mode of the velocity pdf for the entire year (triangles). Deep gravity busts (such as YD 176, green) and ultragravity booms (YD 239, red, is one of the largest) are clearly distinguished from the normal spectrum. Velocity spectra (solid, referenced to the left axis) and pressure (dash, referenced to the right axis) are in overall accord and lend confidence to our interpretation.

For several hours surrounding the time window of the normal day, both wind models indicate speeds overhead of 4.5–5 m s^{-1}, a little less than the annual average, and at the low end of the speed required for saturation in the gravity band. At the time of the maximum bust, the speed was in the range 2.6–2.8 m s^{-1}. At the time of the maximum boom, the CCMP wind was 14.8 m s^{-1}, but it was missed by the NCEP model.

Gravities saturate for wind speed above 5–6 m s^{-1}, while ultragravities do not saturate in this range. It follows that the exact $g|ug$ transition frequency depends on wind speed. Although nominally 5 Hz, it drops below 4 Hz for 14 m s^{-1} winds (Fig. 4, red curves) and rises to about 6 Hz as the wind drops below 6 m s^{-1}. For very low winds, the ultragravity spectrum appears to saturate (see Fig. 5). This effect may not be real, because the spectra at these frequencies and under these wind

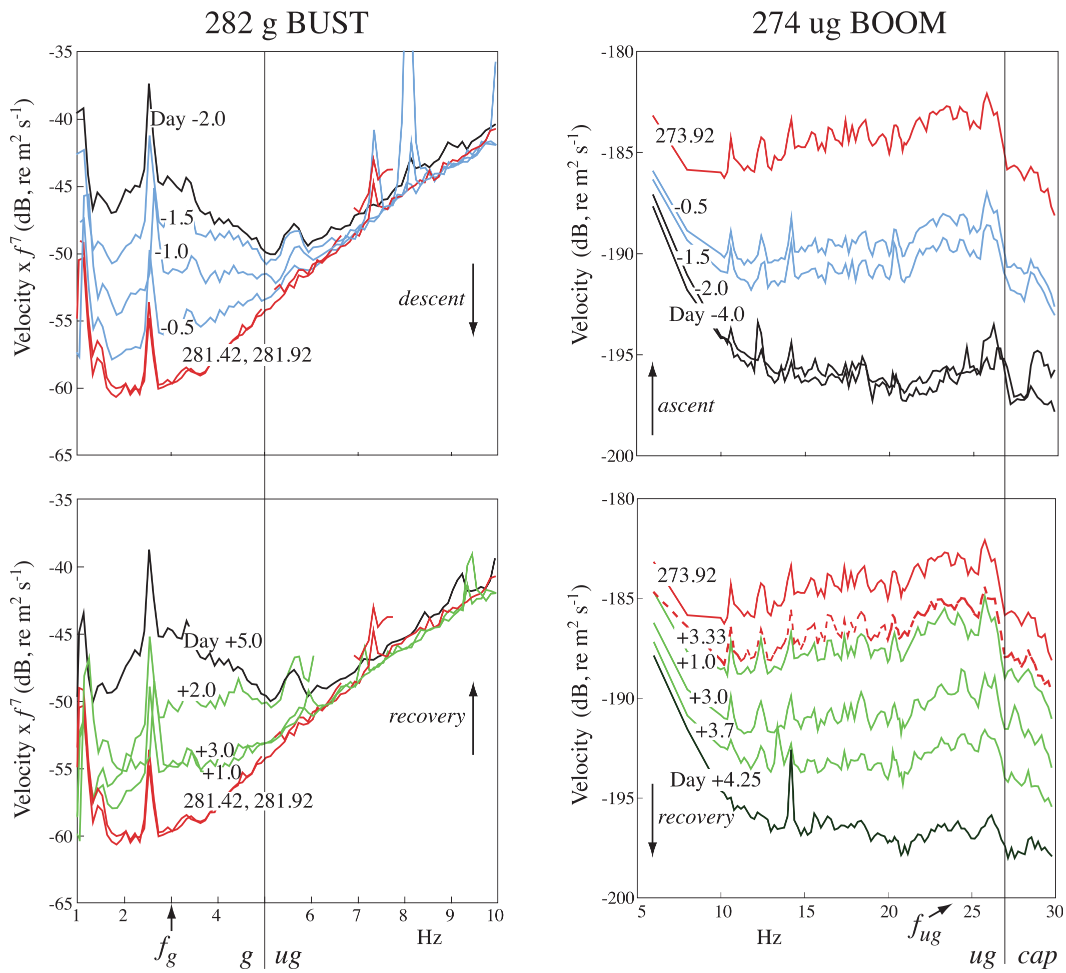

FIG. 2. Spectra of a bust (flattened by $10^{-4} f^7$) and boom at selected times. Initial and final states (black) are virtually identical and are typical of the normal spectrum (see Fig. 4).

conditions are close to the instrument noise floor. Some estimates of acoustic transition frequency and corresponding wave parameters are given in Table 1.

A change in the slope of the deep ambient pressure spectrum in the neighborhood of 5 Hz has long been known in the acoustic community (Kibblewhite and Ewans 1985, Fig. 9). We associate this transition to a transition centered near 2.5 Hz in the spectrum of surface waves. The deep-water gravity wave dispersion relation yields 4 cpm or 25-cm wavelength (Table 1). There is an extensive literature on waves 1 m or longer, and measured spectra are in accord with the Phillips (1958) model of saturated (wind independent) spectral densities. Very little is known about surface waves 25 cm and shorter. However, there is good evidence that short waves, unlike the gravities, are not saturated under strong winds. Our inference of a transition wavelength of about 25 cm at low winds is consistent with Heron et al. (2006, Fig. 7), which is based on the discussion of Elfouhaily et al. (1997, section 6.3). For the three wind speeds shown in Table 1, our estimates of the transition wavelength are about half Heron et al.'s.

We return to a discussion of the relation between surface and bottom spectra in the next section. Here we continue an interpretation of the H2O data. A quantitative relation between wind speed and bottom velocity is required, and this is derived from the data plotted in Fig. 5. We focus on the gravity band, top panel, which shows the scatterplot of CCMP wind speed versus intensity at 3 Hz for the year.

The 3-Hz power rises at 3.3 dB (m s^{-1})$^{-1}$ until saturation is reached, and we take this to occur exactly at 6 m s^{-1}. The imprecision in the slope is largely due to imprecision in the wind data. The two wind models differ, on average, by about 1 m s^{-1}, which is on the order of the horizontal scatter for low winds. Furthermore, for winds greater than 6 m s^{-1}, where the intensity is independent of wind speed, the scatter in the vertical

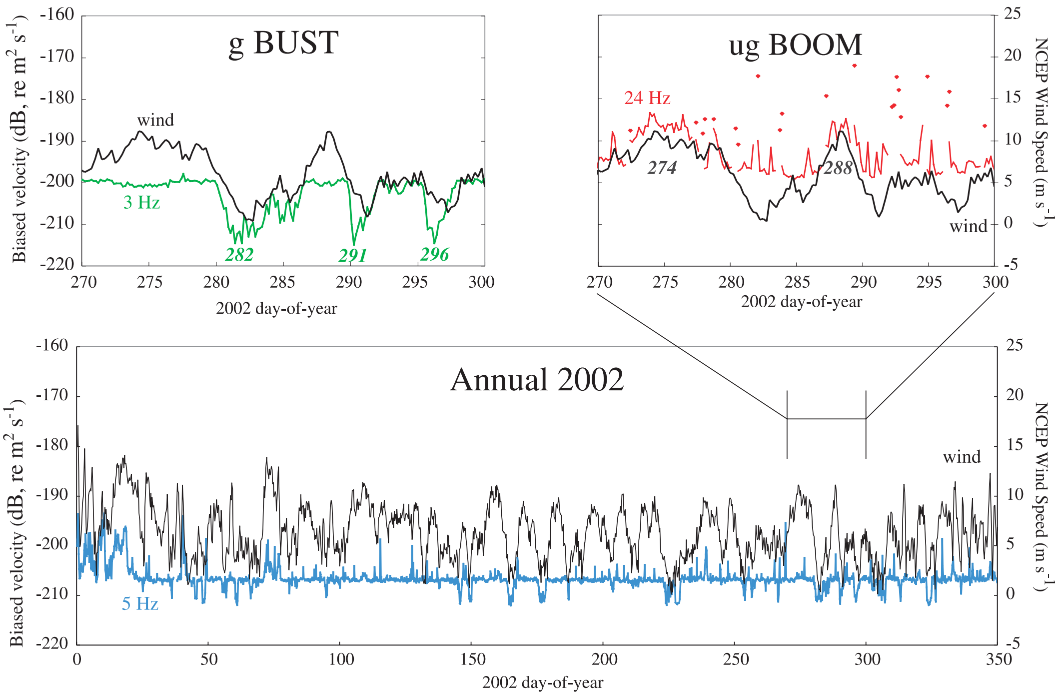

FIG. 3. A 30-day time history of bottom busts (at 3 Hz; green) and booms (24 Hz; red) is highly correlated with surface winds (black). Note the recovery to pre-event levels. The 24-Hz signals are frequently contaminated by shipping noise (red dots). (bottom) The intermediate frequency of 5 Hz (blue) is only weakly correlated with wind speed for the entire year. (The velocity axis has been adjusted to align the pair of traces and is not the true power at the stated frequency.)

(velocity) coordinate is just a few decibels. If this small velocity scatter holds at the lower wind speeds, then virtually all the spread is attributable to the wind, not the spectral intensity.

A similar result is obtained at other frequencies in the gravity band and for H2O pressure as well. Pressure data like those shown in Fig. 5 have appeared previously in the literature (e.g., McCreery et al. 1993, Fig. 12).

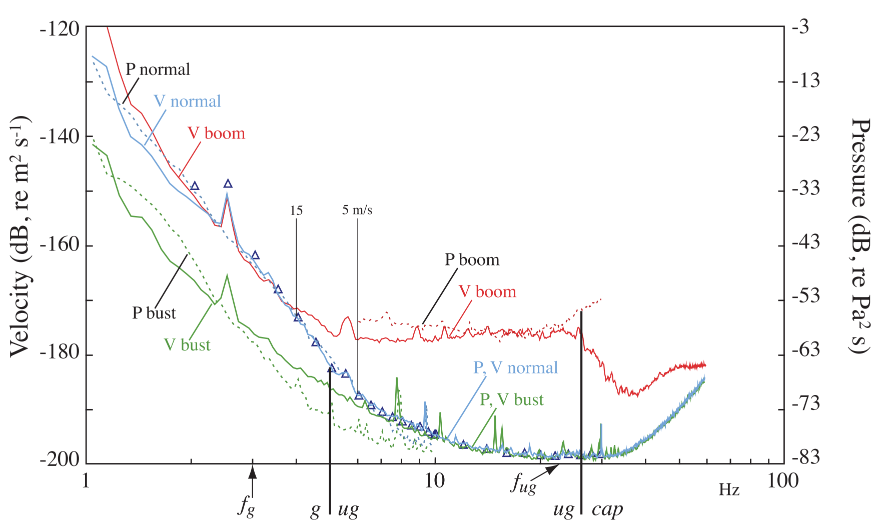

FIG. 4. Spectra of velocity (solid lines; left axis) and pressure (dashed lines; right axis) for normal conditions on YD 201 (blue), a bust on YD 176 (green), and a boom on YD 239 (red). Triangles designate the velocity modes for the entire year (see text).

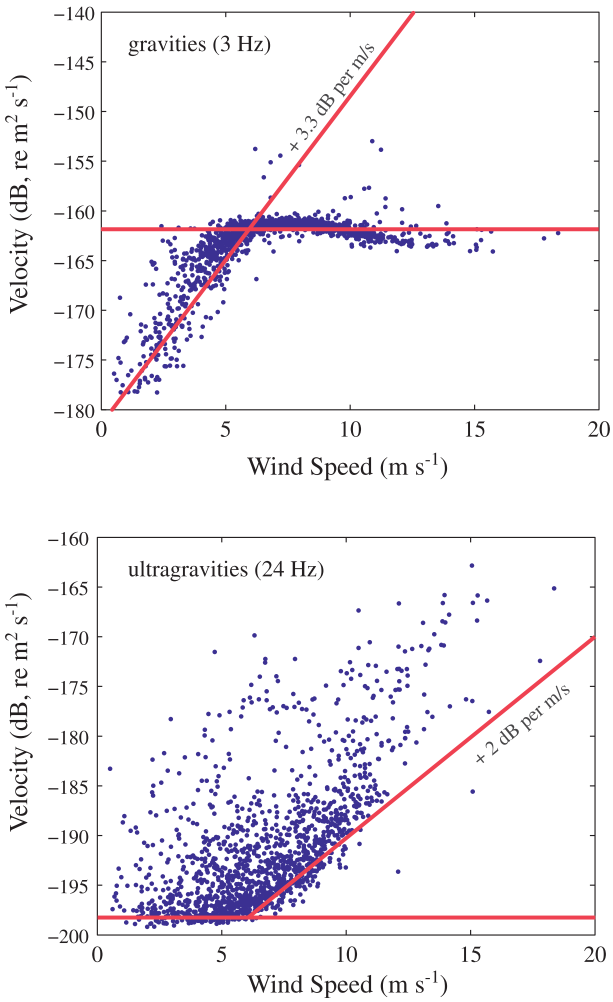

FIG. 5. Six-hourly mean of surface wind and bottom velocity for the entire year at (top) 3 and (bottom) 24 Hz. The former show the characteristic signatures of gravity busts, with saturation for $U >$ 6 m s^{-1}; the latter of ultragravity booms with saturation for $U <$ 6 m s^{-1} (see text).

The slope discontinuity in both scatterplots near $U =$ 6 m s^{-1} is striking. At this wind speed, the gravities settle against the saturation ceiling and the ultragravities begin to lift off their spectral floor. The break in the scatterplot of the gravities is real and may well be associated with the initiation of wave breaking, as suggested by McCreery et al. (1993). The break in the scatterplot of the ultragravities, though tantalizingly near the same wind speed, may be due to sensor noise, not wave physics.

We note that an estimate of wind at a point is being used in the comparisons, and that estimate is based on an interpolation of an assimilation model with some grid spacing. Typical grid intervals range from 25 to 100 km. In fact, the pressure and velocity fluctuations are induced by the average wave field over a sizable patch of ocean above. In the case of homogeneous waves and using the Green function for a dipole layer, 90% of the power in the velocity field is generated within a radius of 3 water depths (15 km) of the overhead point. For pressure, the 90% limit is 5 water depths (25 km).

TABLE 1. Parameters for the $g|ug$ transition estimated from deep sea observations.

U (m s^{-1})	f_{ac} (Hz)	f_{wave} (Hz)	λ_{wave} (cm)
15	4	2	40
10	5	2.5	25
≤6	6	3	17

4. Relation between surface and bottom spectra

The ocean wave model devised by Farrell and Munk (2008) to interpret the spectra of one Wake Island hydrophone works equally well for the H2O hydrophone and fits the geophone data to about the same accuracy. In the gravity band, between the wind cutoff κ_U and the $g|ug$ transition κ_1, the amplitude spectrum is

$$\left.\begin{aligned} &F_\zeta(f,\theta) = 2\pi g^2\beta(2\pi f)^{-5}H(\theta), \quad \int d\theta H(\theta) = 1 \\ &f_U \le f \le f_1 \\ &f_U = g/(2\pi U), \quad f_1 = 2.5\,\mathrm{Hz} \pm \delta f(U) \end{aligned}\right\}, \qquad (1)$$

where $f = \omega/2\pi$ is the cyclic frequency. The top panel of Fig. 6 shows F_ζ integrated over all directions.

Equation (1) has one free parameter, the Phillips constant β, and leaves the spread function H undetermined. For the integrated spectrum, we take $F_\zeta = -33$ dB at 1 Hz as representative of the range of values given by Banner (1990, Fig. 6), which specifies $\beta = 0.008$. Above $f_1 \approx 2.5$ Hz, the ultragravities, with less than f^{-5} slope, dominate the gravities. The shape of the ultragravity spectrum is not well determined by surface observations. We can go to the bottom pressure spectrum for guidance.

The bottom panel of Fig. 6 plots the acoustic pressure spectrum at frequencies twice the wave frequency. Substituting the preceding wave model into the expression for the acoustic radiation, the pressure in the gravity band, far from the surface in a bottomless ocean, is given by (e.g., Farrell and Munk 2008)

$$\left.\begin{aligned} &F_P(f) = 8\pi^2\left(\frac{\rho g^3}{c}\right)^2(\pi f)^{-7}\beta^2 I(f), \\ &I = \int d\theta H(\theta)H(\theta+\pi) \\ &2f_U \le f \le 2f_1 \end{aligned}\right\}. \qquad (2)$$

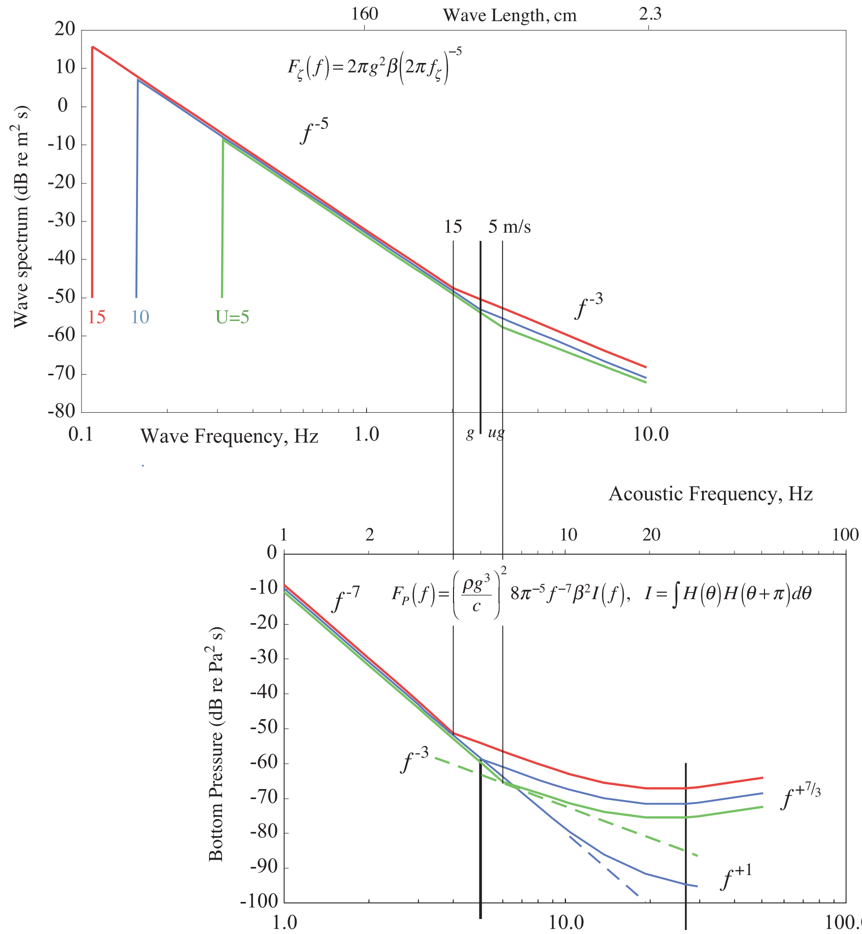

FIG. 6. Schematic of the relation between surface wave and bottom pressure spectra. For normal condition (no boom or bust), both surface and bottom spectra are saturated (colored lines, closely bunched) for the gravity waves. At higher frequencies, the spectra change slope and become wind dependent, marking the transition from gravities to ultragravities, as shown. H2O pressure spectra, with transition from f^{-7} to f^{-3}, are roughly consistent with a transition of the surface spectra from the Phillips f^{-5} g spectrum to an f^{-3} ug spectrum.

Equation (2) has one free function, the overlap integral I. For $I = (2\pi)^{-1}$, as appropriate for an isotropic spread function, $F_P(1\ \text{Hz}) = -10$ dB. This is representative of the range of values given in the literature.

It is encouraging that the bottom pressure measurements in the gravity band are consistent with the surface spectra with regard to both slope and intensity. The velocity spectra have the same f^{-7} slope expected for the bottomless ocean model. The level of the velocity spectra can be derived from the level of the pressure spectra by a simple acoustic argument. For a plane wave, velocity is related to pressure by the acoustic impedance ($Z = \rho c$), so the spectra are related by its square, $F_P/F_V = Z^2$. On account of the directional sensitivity of the geophone, the velocity signature is halved when the energy comes from a dipole surface layer, so $F_P/F_V = 2Z^2 = 126.5$ dB, using the impedance of seawater. With bottom-based instruments, the character of the seafloor will affect the ratio which, in general, will depend on frequency. These effects seem to be secondary, because Fig. 4 showed that the spectra of pressure and velocity were roughly parallel and that the same spectral shift, 117 dB, accommodated the difference between pressure and velocity for all three cases.

The situation is more complex for the ultragravity band (Farrell and Munk 2008). However, far away from the $g|ug$ transition, the bottom pressure and velocity can be tolerably fitted by wind-dependent lines of slope f^{-3}. Working backward, the bottom spectra infer the wind-dependent surface spectra as shown (again of slope f^{-3}), and these are not inconsistent with the scant surface measurements.

5. Directional beam model and associated integrals

For further discussion, we require a model of directional spread. Three of the most widely used models are (i) $\cos^{2s}(\theta/2)$ introduced by Longuet-Higgins et al. (1963), (ii) $\mathrm{sech}^2(\beta\theta)$ introduced by Donelan et al. (1985), and (iii) the bimodal Gaussian introduced by Ewans (1998). There is convincing evidence that the spread function of the gravities becomes bimodal for wavenumbers more than 10 times the wind cutoff (e.g., Hwang and Wang 2001, Fig. 4). We chose two Gaussian beams in the directions $\pm\theta^*$ relative to the mean wind direction, each with standard deviation (or spread) σ. This is simple and traditional, with the merit of permitting analytical evaluation of all integrals involved. Our experience with other bimodal models suggests that the overall topology is not sensitive to the model details.

The directional spectrum $H(\theta;\, \theta^*, \sigma)$ is

$$H = N^{-1}\left[\exp\left(-\frac{(\theta-\theta^*)^2}{2\sigma^2}\right) + \exp\left(-\frac{(\theta+\theta^*)^2}{2\sigma^2}\right)\right], \qquad (3)$$

with normalization

$$N = \sqrt{2\pi}\sigma\left[\mathrm{Erf}\left(\frac{\pi-\theta^*}{\sqrt{2}\sigma}\right) + \mathrm{Erf}\left(\frac{\pi+\theta^*}{\sqrt{2}\sigma}\right)\right]. \qquad (4)$$

The boundary $\sigma_{\mathrm{crit}}(\theta^*)$ between unimodal and bimodal distributions is determined by $H_{\theta\theta}(0,\, \theta^*, \sigma) = 0$ (subscripts denote differentiation), yielding $\sigma = \theta^*$, with unimodal distributions for $\sigma > \theta^*$ and bimodal distributions for $\sigma < \theta^*$.

Fluctuations on the deep seafloor require oppositely traveling wave energy and are proportional to the "overlap integral" defined in (2),

$$I(\theta^*, \sigma) = \int_{-\pi}^{\pi} d\theta H(\theta;\, \theta^*, \sigma) H(\theta + \pi;\, \theta^*, \sigma). \qquad (5)$$

The integral is a complex function of many error functions, and we have found it preferable to evaluate it numerically. Contour levels of I are shown in the top panel of Fig. 7.

The ratio of crosswind to upwind/downwind mean-square slope is given by

$$J(\theta^*, \sigma) = \frac{\displaystyle\int_{-\pi}^{\pi} d\theta H(\theta;\, \theta^*, \sigma)\sin^2\theta}{\displaystyle\int_{-\pi}^{\pi} d\theta H(\theta;\, \theta^*, \sigma)\cos^2\theta}. \qquad (6)$$

Contour levels of J are shown in the bottom panel of Fig. 7. Information concerning the J ratio also comes from satellite measurements of sun glitter.

The space in the I and J planes is divided by $\sigma = \theta^*$ into two regions derived from the spread function H, which are unimodal and bimodal, respectively. The limit $\sigma = 0$ is associated with two pencil beams (overlapping for $\theta^* = 0$) and $\sigma = \infty$ with directional isotropy [$I = (2\pi)^{-1}$ or -7.98 dB]. We have taken the right y axis in both figures as linear in the function $b(\sigma) = \sigma/(1 + \sigma)$ so that $\sigma = 0$, $b = 0$ corresponds to delta beams and $\sigma = \infty$, $b = 1$ corresponds to directional isotropy.

6. Interpretation of a bust

The premise here is that the bust in the spectrum of the bottom geophone and hydrophone recordings is associated with a reduction at low wind speeds in the wind angle θ^* and the spread σ, leading to a precipitous reduction in oppositely traveling wave energy. The reduction in the overlap integral is entirely caused by interference between wave components generated by overhead winds [see Eq. (2)]. At these wavelengths, viscous dissipation makes it unlikely that interference between waves from separated source regions (e.g., swell) can be an important source of the acoustic radiation.

The surface spectrum is saturated and its spectral density is independent of wind speed, provided the wind U exceeds the phase speed C; for a 1.5-Hz gravity wave (3-Hz bottom frequency), the phase velocity for $U = C$ is 1 m s^{-1} and less than the lowest recorded wind speed. Accordingly, the surface spectra are saturated and independent of wind speed, whereas the bottom spectra (pressure or velocity) are proportional to the wind-dependent overlap integral $I(\theta^*, \sigma)$.

Figures 2 and 3 illustrate the situation for the bust centered on YD 282: there is a drop of the bottom velocity spectrum at 3 Hz of roughly 15 dB for winds dropping from 5 to 2 m s^{-1}. Perhaps more significant is the lack of a further spectral enhancement as the wind rises up to 15 m s^{-1} (Fig. 5). Thus, the bottom spectrum is unsaturated for low winds (unlike the surface spectrum), but both bottom and surface spectra are saturated for moderate and high winds.

Our interpretation is that the overlap integral comes within a few decibels of isotropy (-7.98 dB) for moderate winds (Fig. 7). To make this quantitative, we compute a typical bust orbit as follows:

$$I(U) = I[\theta^*(U), \sigma(U)], \qquad (7)$$

or equivalently

$$\mathrm{dB}(U) = \mathrm{dB}[\theta^*(U), \sigma]. \qquad (8)$$

The left side is derived from the annual scatter diagram (Fig. 5). We assume isotropy for $U > 6$ m s^{-1}, in which

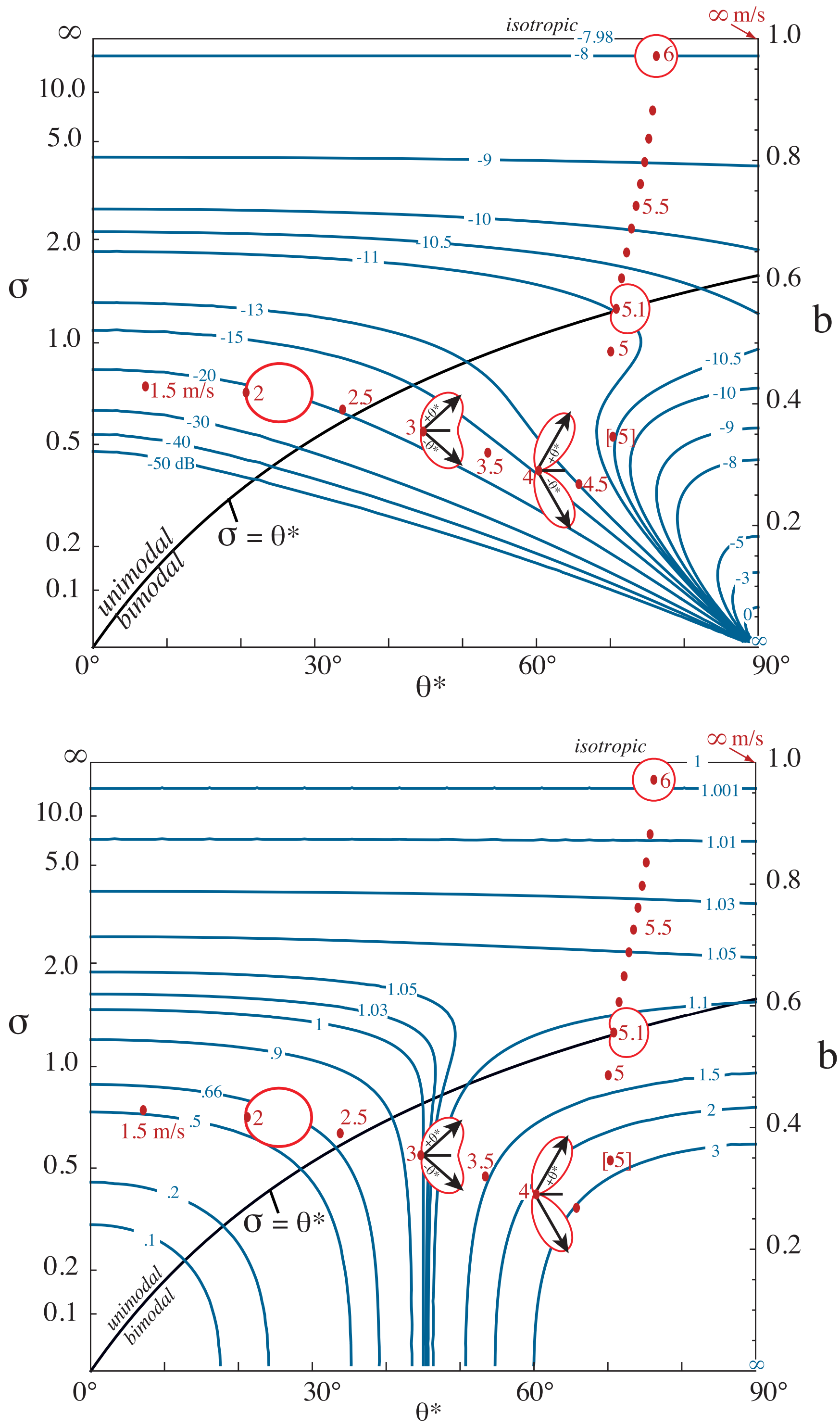

FIG. 7. Contours (top) of the overlap integral $I(\theta^*, \sigma)$ and (bottom) of J, the ratio $\langle m_y^2\rangle/\langle m_x^2\rangle$ of crosswind to along-wind components of mean-square slope for two Gaussian beams with spreads σ in directions $\pm\theta^*$ relative to the wind [Eq. (3)]. Here, σ extends from 0 to ∞ and is plotted linearly with scale $b = \sigma/(1 + \sigma)$ from 0 to 1. The beams are bimodal for $\sigma < \theta^*$ and unimodal for $\sigma > \theta^*$, as shown. Here, $\sigma = 0$ corresponds to two pencil beams at $\pm\theta^*$. For $\sigma = \infty$ ($b = 1$), the beam is directionally isotropic with $I = -7.98$ dB. The ratio J is 0 for $\theta^* = 0, \sigma = 0$ and 1 for $\sigma = \infty$. Red points show the orbit of a gravity wave bust of frequency 3 Hz at the indicated wind speeds. Red insets give the directional beam pattern $H(\theta; \theta^*, \sigma)$ in polar coordinates (but with Cartesian normalization) at five stages of the bust. The orbit is multivalued at 5 m s^{-1}.

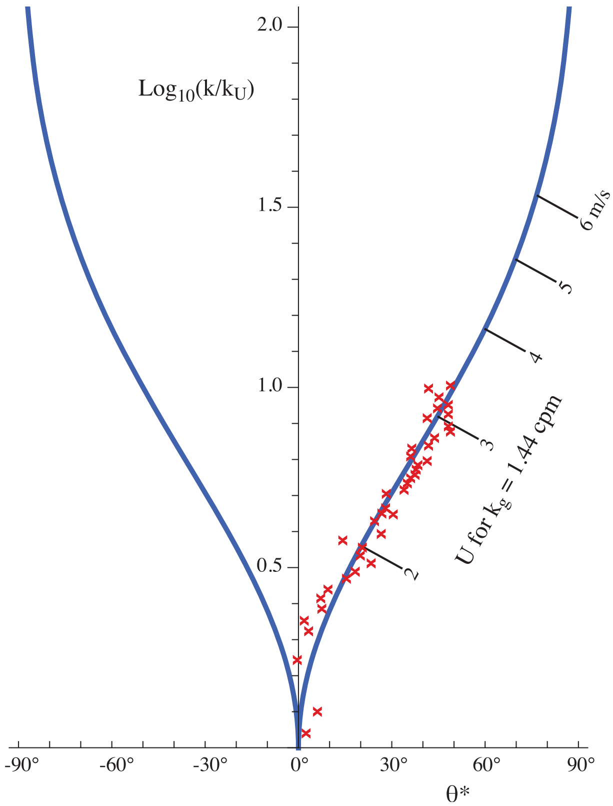

FIG. 8. Angular departure from the downwind direction of $\theta^*(k/k_U)$ according to (10). Crosses are data collected by Ewans (1998) under fetch-limited conditions and taken from Heron et al. (2006). Here, $k = 1.44$ cpm, corresponding to a frequency of 1.5 Hz (3 Hz acoustic) and $k_U = g/(2\pi U^2)$ for the wind cutoff wavenumber (assuming $C = U$). The wine glass fit has been wildly extrapolated to $\theta^* = 90°$ for $k/k_U = \infty$.

case $I \approx -8$ dB; for lesser winds, the intensity approaches -8 dB at the rate 3.3 dB per m s^{-1}. Thus,

$$\left.\begin{aligned} \mathrm{dB}(U < 6\,\mathrm{m\,s^{-1}}) &= -28 + 3.3U \\ \mathrm{dB}(U > 6\,\mathrm{m\,s^{-1}}) &= -8\,\mathrm{dB} \end{aligned}\right\}. \tag{9}$$

The relation $\theta^*(U)$ (Fig. 8) is obtained by fitting the data of Ewans (1998), as redrawn in Heron et al. (2006, Fig. 6), to the curve

$$\left.\begin{aligned} &\theta^*(y) = \pm\frac{1}{2}\pi[1 - \exp - (hy)^2], \quad h = 0.9, \\ &\quad y = 2\log_{10}(f/f_U), \quad f = 1.5\,\mathrm{Hz}, \quad f_U = g/(2\pi U) \end{aligned}\right\}, \tag{10}$$

where $f = 1.5$ Hz is the selected surface wave frequency (3-Hz bottom frequency) and f_U is the wind cutoff frequency (peak energy) derived from $C = U$. This gives $\theta^*(U)$. Thus, with dB(U) and $\theta^*(U)$ known, Eq. (8) is in the form $F(U, \sigma) = 0$ and yields $\sigma(U)$. For any selected U, we obtain a point in θ^*, σ space (red points in Fig. 7). This determines the bust orbit.

We can now identify the orbits with the required directional beam pattern. Starting with a nearly isotropic beam at high and moderate winds, the beam turns bimodal and narrow near 4 m s^{-1} and then widens and turns unimodal for winds less than 2.5 m s^{-1}. The initial descent is from σ near 10 to $\sigma = 0.3$, with θ^* remaining near 70°. At very weak winds the reduction in the overlap integral is associated with a nearly tenfold reduction in θ^*, with σ rising from 0.3 to 0.8. The pattern is similar for neighboring frequencies (not shown). At 1 Hz (compared to 1.5 Hz), the initial descent is near $\theta^* = 60°$ (compared to 70°) and the final σ is near 0.9. The beam pattern remains unimodal throughout.

There are many uncertainties here, among them that the "wine glass relation" (Fig. 8) is based on frequencies lower than 3 Hz. However, we are encouraged that, at the upper limit of direct observation of the gravities, $\kappa/\kappa_U = 9$, our beam pattern ($\theta^* = \pm 45°$, $\sigma = 0.5$) does not differ significantly from three results summarized in Hwang and Wang (2001, Fig. 4).

7. Slope ratio

Some recent satellite observations of sun glitter have given reproducible values of the ratio of crosswind to upwind/downwind components of mean-square slope (Bréon and Henriot 2006; Munk 2009). The ratio is near two-thirds for winds between 2 and 15 m s^{-1}. According to Fig. 7, bottom, the ratio does approach something near two-thirds at weak winds; however, at high and moderate winds, the ratio is near or above 1. However, here we need to remind the reader that the glitter measurements refer to the combined slopes of the gravity, ultragravity, and capillary waves.

8. Discussion

The preceding discussion is purely empirical, depending on the evidence from bottom and surface measurements, combined with the assumed Gaussian beam model. Is there any physical principle that leads to a bimodal beam pattern widening with increased wind speed? The Phillips (1958) resonance model provides for just this kind of dependence. In relating the two-dimensional spectrum of surface atmospheric pressure to that of surface waves, he finds that any surface wavenumber κ is in resonance with the κ component of pressure in the direction of the surface waves at an elevation κ^{-1}. This leads directly to the postulated beam pattern. It may seem counterintuitive that so much of the energy travels at nearly a right angle to the wind. In the related ship wave problem (Lamb 1932, p. 434), most of the mean-square slope is associated with bow waves that move at nearly a right angle to the ship's course.

We have described some of the features of gravity waves of 2–50-cm lengths using measurements of pressure and velocity on the deep sea floor. At first glance, this would appear an unlikely place to look for information about short surface waves. However, direct measurements on a rough sea surface are difficult, and the analysis of resolved surface images is complex and subject to great frame-to-frame variability.

Consider a hydrophone at 5-km depth responding to distributed surface sources. The pressure measurement will be responsive to sources within a circle centered over the hydrophone and of radius equal to several depths, say 10 km. At a wavelength of 10 cm, the generating area is $3 \times 10^{10}\lambda^2$.

Our bottom spectra are typically based on $T = 4$ h records. For $\Delta f = 0.1$ Hz resolution, this corresponds to $2\Delta fT \approx 3000$ degrees of freedom in the frequency domain. This combination of spatial and temporal averaging accounts for the remarkable stability of the bottom measurements, equivalent to the analysis of very large numbers of surface images. In closing, we may be permitted to quote Tyler et al. (1974): "the monitoring of pressure fluctuations on the deep sea bottom could provide some further information on the [surface wave] directional spectrum."

Acknowledgments. We had the benefit of many discussions with C. Cox, K. Melville, and M. Longuet-Higgins. Xavier Zabalgogeazcoa, of SAIC, helped in many ways, not least by calculating the spectra. Xavier also devised the scaling law behind Fig. 1 and provided the images. Brian Sperry provided the CCMP wind data and the images for Fig. 5; Nicholas Graham provided the NCEP winds, as well as wave estimates. John Bourdelais, Charles Spofford, and Zachary Guralnik were influential. Fred Duenebier gave us detailed information about the H2O instrumentation. W. E. Farrell was partly supported by SAIC, and Walter Munk has the Secretary of the Navy Chair in Oceanography.

REFERENCES

Atlas, R., J. Ardizzone, and R. N. Hoffman, 2008: Application of satellite surface wind data to ocean wind analysis. *Remote Sensing System Engineering,* P. E. Ardanuy and J. J. Puschell, Eds., International Society for Optical Engineering (SPIE Proceedings, Vol. 7087), doi:10.1117/12.795371.

Banner, M. L., 1990: Equilibrium spectra of wind waves. *J. Phys. Oceanogr.,* **20,** 966–984.

Brekhovskikh, L. M., 1966: Underwater sound waves generated by surface waves in the ocean. *Izv. Acad. Sci. USSR Atmos. Oceanic Phys.,* **2,** 970–980.

Bréon, F. M., and N. Henriot, 2006: Spaceborne observations of ocean glint reflectance and modeling of wave slope distributions. *J. Geophys. Res.,* **111,** C06005, doi:10.1029/2005JC003343.

Donelan, M. A., J. Hamilton, and W. H. Hui, 1985: Directional spectra of wind-generated waves. *Philos. Trans. Roy. Soc. London,* **315A,** 509–562.

Duennebier, F. K., D. W. Harris, J. Jolly, J. Babinec, D. Copson, and K. Stiffel, 2002: The Hawaii-2 Observatory seismic system. *IEEE J. Oceanic Eng.,* **27,** 212–217.

Elfouhaily, T., B. Chapron, K. Katsuros, and D. Vandemark, 1997: A unified directional spectrum for long and short wind-driven waves. *J. Geophys. Res.,* **102,** 15 781–15 796.

Ewans, K. C., 1998: Observations of the directional spectrum of fetch-limited waves. *J. Phys. Oceanogr.,* **28,** 495–512.

Farrell, W. E., and W. Munk, 2008: What do deep sea pressure fluctuations tell about short surface waves? *Geophys. Res. Lett.,* **35,** L19605, doi:10.1029/2008GL035008.

Heron, M. L., W. J. Skirving, and K. J. Michael, 2006: Short-wave ocean wave slope models for use in remote sensing data analysis. *IEEE Trans. Geosci. Remote Sens.,* **44,** 1962–1973.

Hwang, P. A., and D. W. Wang, 2001: Directional distributions and mean square slopes in the equilibrium and saturation ranges of the wave spectrum. *J. Phys. Oceanogr.,* **31,** 1346–1360.

Kalnay, E., and Coauthors, 1996: The NCEP/NCAR 40-Year Reanalysis Project. *Bull. Amer. Meteor. Soc.,* **77,** 437–471.

Kedar, S., M. Longuet-Higgins, F. Webb, N. Graham, R. Clayton, and C. Jones, 2008: The origin of deep ocean microseisms in the North Atlantic Ocean. *Proc. Roy. Soc. London,* **464A,** 777–793.

Kibblewhite, A. C., and K. C. Ewans, 1985: Wave-wave interactions, microseisms, and infra-sonic ambient noise in the ocean. *J. Acoust. Soc. Amer.,* **78,** 981–994.

——, and C. Y. Wu, 1996: *Wave Interactions as a Seismo-Acoustic Source*. Springer-Verlag, 313 pp.

Lamb, 1932: *Hydrodynamics*. 6th ed. Cambridge University Press, 738 pp.

Longuet-Higgins, M. S., 1950: A theory of microseisms. *Philos. Trans. Roy. Soc. London,* **243,** 1–35.

——, D. E. Cartwright, and N. D. Smith, 1963: Observations of the directional spectrum of sea waves using the motions of a flotation buoy. *Ocean Wave Spectra,* Prentice-Hall, 111–136.

McCreery, C. S., F. K. Duennebier, and G. H. Sutton, 1993: Correlation of deep ocean noise (0.4–30 Hz) with wind, and the Holu Spectrum—A worldwide constant. *J. Acoust. Soc. Amer.,* **93,** 2639–2648.

Munk, W., 2009: An inconvenient sea truth: Spread, steepness and skewness of surface slopes. *Annu. Rev. Mater. Sci.,* **1,** 377–415.

Phillips, O. M., 1958: The equilibrium range in the spectrum of wind-generated waves. *J. Fluid Mech.,* **4,** 426–434.

Tyler, G. L., C. C. Teague, R. H. Stewart, A. M. Peterson, W. H. Munk, and J. W. Joy, 1974: Wave directional spectra from synthetic aperture observations of radio scatter. *Deep-Sea Res.,* **21,** 989–1016.

Webb, S. C., and C. S. Cox, 1986: Observations and modeling of seafloor microseisms. *J. Geophys. Res.,* **91,** 7343–7358.